Available online at www.sciencedirect.com
ScienceDirect
Acta Materialia 55 (2007) 5822–5832
Acta MATERIALIA
www.elsevier.com/locate/actamat

Optimizing the strength and ductility of fine structured 2024 Al alloy by nano-precipitation

S. Cheng [a,*], Y.H. Zhao [b], Y.T. Zhu [b], E. Ma [a]

[a] Department of Materials Science and Engineering, The Johns Hopkins University, Baltimore, MD 21218, USA
[b] Materials Science and Technology Division, Los Alamos National Laboratory, Los Alamos, NM 87545, USA

Received 4 February 2007; received in revised form 16 June 2007; accepted 26 June 2007
Available online 27 August 2007

Abstract

Alloys with grain or subgrain structures refined down to 1 μm or below usually have high strength, but often inadequate tensile ductility. Past efforts in improving their ductility have usually led to a sacrifice of strength. We have developed an effective approach in achieving both high strength and high ductility in a 2024 Al alloy. The approach involves solution-treatment to partially dissolve T-phase particles, cryo-rolling to produce a fine-structure containing a high density of dislocations and submicrometer subgrains and aging to generate highly dispersed nano-precipitates. It was found that the remnant T-phase particles made it very effective in accumulating dislocations during cryo-rolling, which in turn promoted the precipitation of nanosized S′ precipitates with an interparticle spacing of only 10–20 nm. Such a high density of S′ precipitates enabled effective dislocation pinning and accumulation, leading to simultaneous increases in strength, work-hardening ability and ductility.

Keywords: Grain refinement; 2024 Al alloy; Cryo-rolling; Precipitation; Tensile ductility

1. Introduction

There has been a strong push to refine the grains or subgrains of metals into the submicrometer and nanocrystalline regimes. Such metals typically have high strength, but their inadequate ductility has become a major issue in their practical application. In recent years, a number of methods have been developed to improve the tensile ductility [1–16]. While most of the earlier approaches improved ductility at the expense of yield strength (e.g., Ref. [3]), a few most recent approaches have succeeded in simultaneously achieving high strength and ductility. One such successful approach involves nano-precipitation hardening in 7075 Al alloy [15]. The processing steps in this approach include: (1) solution-treating the Al alloy to dissolve all second-phase particles and to produce an oversaturated solid solution; (2) cryo-rolling at liquid nitrogen temperature to produce ultrafine-grained (UFG) microstructures, and (3) aging to produce highly dispersed second-phase nano-sized particles. It should be noted that similar precipitation approaches were also attempted earlier and produced good combinations of high strength and ductility [17–21,12], although no simultaneous increases in strength and ductility were achieved or verified. For instance, equal-channel angular pressing (ECAP) has been applied to different Al alloy systems to obtain high strength and ductility [19–21,12,22]. Kim et al. reported that by combining solid solutioning, ECAP and post-ECAP low-temperature aging, the yield strength of 2024 Al alloy was improved to ~630 MPa while maintaining a respectable ~15% elongation to failure. However, their study did not explore much on the mechanism [21]. Horita et al. studied the effect of post-ECAP low-temperature aging on tensile behavior of Al–10.8 wt.%Ag alloy [10]; by high-resolution transmission electron microscopy

* Corresponding author. Present address: Department of Materials Science and Engineering, University of Tennessee, Knoxville, TN 37996, USA. Tel.: +1 865 974 2683; fax: +1 865 974 4115.
E-mail address: scheng1@utk.edu (S. Cheng).

1359-6454/$30.00
doi:10.1016/j.actamat.2007.06.043

(HRTEM), they revealed that work hardening can be improved by producing fine "η-zone" precipitate particles with sizes <50 nm dispersed in the grain volume.

In all of the foregoing investigations, the second-phase particles were mostly or completely dissolved into the matrix to produce a supersaturated solid solution. This may not be desirable for some Al alloys. For example, the high concentrations of alloying elements in the 2024 Al alloy render the alloy very brittle if all of the second-phase (T-phase) particles are dissolved into the matrix, making it very difficult or impossible to refine its grains by plastic deformation methods such as cryo-rolling or ECAP. In addition, if one leaves some second-phase particles undissolved, they could play a positive role in promoting dislocation accumulation and grain refinement during the severe plastic deformation step. This, if proved true, may in turn promote the precipitation of nano-sized second-phase particles during aging, which may further enhance both the strength and ductility by resisting dislocation slip and trapping dislocations.

It was the objective of this study to develop an improved procedure for simultaneously enhancing the strength and ductility of age-hardening Al alloys. In this approach, we aimed to only partially dissolve the second-phase particles during the solution treatment to improve the processability and to enhance the precipitation of nano-sized second-phase particles. We used 2024 Al-alloy in this study because it represents a type of alloys that are brittle if the second-phase particles are completely dissolved. In addition, our investigation on the 2024 Al alloy systematically adjusted the processing parameters to obtain the optimized strength and ductility.

2. Experimental procedure

Commercial 2024 Al alloy bars were purchased from Alfa Aesar, with a composition of 4.5 wt.%Cu–1.5 wt.%Mg–0.5 wt.%Mn–balance Al. The as-received alloy was first solid-solution treated at a temperature in the range of 493–540 °C for 1–10 h and then quenched in water to room-temperature [23–26]. Such samples are referred to as the solid-solution-treated (SST) samples hereafter. The SST samples were subsequently cryo-rolled (CR) at liquid nitrogen temperature (LN_2T) to a rolling strain up to ~100% (rolling strain $\varepsilon_r = (S_0 - S)/S$, where S_0 and S are the cross-sectional areas before and after rolling [11]), with <5% for each rolling pass. The samples processed by cryo-rolling will be referred to as the fine-structured samples hereafter because of their refined subgrain structure after processing. Temperature was monitored before and after each rolling pass and the temperature after each pass was below –150 °C. Alternate rolling along the longitudinal and transverse directions was used to avoid severe grain elongation. For the purpose of comparison, room temperature (RT) rolling was also conducted. Different schemes of aging were conducted at 100–200 °C for up to 150 h to optimize the strength/ductility combination. Vickers hardness was measured to keep track of the hardness variation. Specimens with a gage length of 6 mm, a thickness of ~0.5 mm and a width of 3 mm were used for tensile testing, which was carried out at a strain rate of 5×10^{-4} s^{-1}. Microstructures were examined using transmission electron microscopy (TEM). *Post-mortem* TEM specimens were cut from the gage section of tensile samples. Energy dispersive spectroscopy (EDS) was used to determine the composition of the precipitates under TEM. High-resolution TEM (HRTEM) was performed to study the precipitate morphology and the dislocation/precipitate interactions. All of the TEM specimens were prepared using jet polishing with a solution of 20% nitric acid +80% methanol at -45 ± 5 °C. TEM observations were carried out using a Philips EM420 microscope operated at 120 kV. The HRTEM was conducted using a JEOL 3000F microscope operated at 300 kV.

3. Experimental results

3.1. Mechanical behavior

Fig. 1a displays the Vickers hardness variation as a function of rolling strain on SST 2024 Al alloy samples. It is clear that the hardness increased with the rolling strain for both RT rolling and cryo-rolling. However, cryo-rolling at LN_2T is more effective in increasing the hardness than RT rolling. At high rolling strains, the hardness tends to saturate.

Fig. 1b shows the hardness variation with aging time at 160 and 100 °C. In contrast to conventionally processed 2024 Al alloy, which typically shows a two-stage aging characterized by an initial rapid hardness increase followed by a plateau [27–29], the 2024 alloy produced by cryo-rolling exhibited a peak hardness at an aging time of ~12 h without a hardness plateau during aging at 160 °C. Compared to the conventional aging in 2024 Al alloy this is a rather short time for the hardness peak to appear at 160 °C. This suggests that the fine-structure produced by CR enhanced aging kinetics [30]. At an aging temperature of 100 °C, the fine-structured sample showed a different hardness evolution with aging time. Specifically, the hardness increased slightly at the beginning and then decreased at a very slow rate at longer aging times, with the maximum hardness at 30–40 h. It is of interest to note that the maximum hardness for the 160 °C aging is about the same as that for the 100 °C aging. The early onset of hardness peak when aged at 160 °C and broad hardness peak when aged at 100 °C are in contrast to the behavior observed in 2024 Al alloy processed by the conventional SST + aging route, which is discussed elsewhere [31].

Fig. 2 shows the typical tensile stress–strain curves of Al 2024 alloy at different processing states. As shown in the engineering stress–strain curves (Fig. 2a), after solution treatment at 493 °C for 10 h the sample has a yield strength of ~150 MPa, an ultimate tensile strength (UTS) of ~380 MPa and an elongation to failure close to 26%

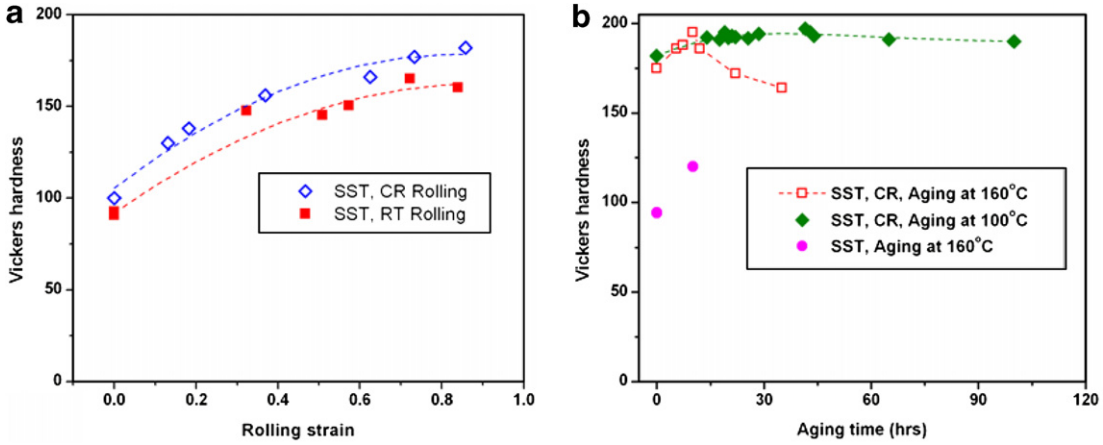

Fig. 1. Vickers hardness of 2024 Al samples. (a) Variations with rolling strain: a higher Vickers hardness was obtained from the CR than from the RT rolling. (b) Variations with aging time at different aging temperatures. The dashed lines in (a) and (b) show the trend lines over the experimental data. CR, cryogenic rolling at liquid nitrogen temperature; RT, room temperature; SST, solid-solution treatment.

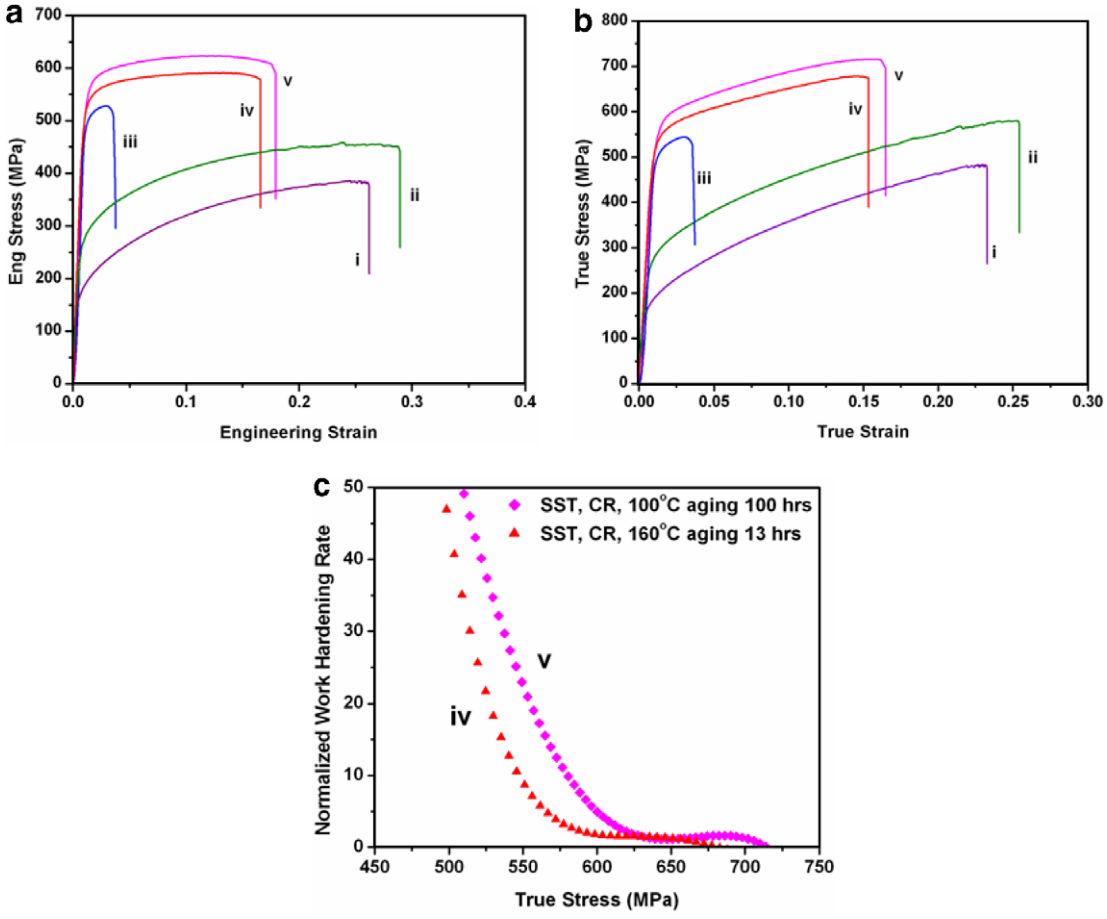

Fig. 2. (a) Typical tensile engineering and (b) the corresponding true stress–strain curves of 2024 Al alloy under different processing conditions. (c) Comparison of the work-hardening rate curves of two types of samples. These curves correspond to different sample processing states: (i) SST at 493 °C; (ii) SST + aging at 160 °C for 10 h; (iii) SST + CR; (iv) SST + CR + aging at 160 °C for 13 h; (v) SST + CR + aging at 100 °C for 100 h.

(curve i). Aging the SST sample at 160 °C for 10 h increased not only the yield strength, but also its ductility (curve ii). Cryo-rolling the SST sample (SST + CR) significantly increased its strength, but reduced its elongation to failure to <5% (curve iii), which is typical of cold-worked metals. Significantly, aging the SST + CR samples dramatically increased their elongation to failure, while modestly further increasing their strength (curves iv and v). It is also

clear that aging at 100 °C for 100 h (curve v) yielded higher strength and ductility than aging at 160 °C for 13 h (curve iv). The yield strength in curve (v) is ~580 MPa, which is more than three times that in curve i for the SST samples and more than twice that in curve ii for the SST + aging samples. Furthermore, curve (v) showed that SST + CR + aging at 100 °C produces an elongation to failure of ~18%, of which ~13% is uniform elongation. These elongations are much larger than those of the SST + CR samples, which are 3.8% and 3.2%, respectively. The uniform elongation is determined by the Considère criterion governing the onset of localized deformation [32,33],

$$\left(\frac{\partial\sigma}{\partial\varepsilon}\right)_{\dot{\varepsilon}} = \sigma \tag{1}$$

where σ is true stress and ε is true strain.

In contrast to most pure nanocrystalline or UFG metals, which often show weak work hardening or even work softening [34–36], the SST + CR + aging samples (curves iv and v) have evident work hardening (Fig. 2b). The normalized work-hardening rate, Θ, ($\Theta = \frac{1}{\sigma}\frac{d\sigma}{d\varepsilon}$), is plotted as a function of true stress in Fig. 2c. As shown, the sample aged at 100 °C has a higher Θ than that in the sample aged at 160 °C, which explains the higher ductility of the former.

Fig. 3a shows tensile strength variations with aging time at 160 °C and 100 °C for the fine-structured samples. When aged at 160 °C, the yield strength and the UTS peaked at an aging time of ~13 h, after which a rapid strength decline followed. Both the yield strength and UTS dropped quickly after the peak and then the drop slowed down at longer aging times. Aging at temperatures higher than 160 °C led to disappointing properties. For example, aging at 180 °C for 5 h led to a low ductility of <10% and a low UTS of ~520 MPa. Therefore, our effort was concentrated on aging at the lower temperatures and higher temperature aging was not studied in detail. By contrast, aging at 100 °C led to high yield strength and UTS, which continued to increase, albeit slowly, with longer aging times. These variations in strengths are consistent with the trend in Vickers hardness shown in Fig. 1b.

Fig. 3b shows tensile elongation-to-failure variation with aging time at 160 and 100 °C. At 160 °C, prolonged aging (>~13 h) also led to low ductility. A minimum elongation-to-failure of ~6% was observed at an aging time of 25 h, after which it recovered to ~8% after aging for 35 h. In contrast, aging at 100 °C led to a tensile elongation-to-failure of ~18% after aging for ~42 h and this slightly increased further with longer aging times.

3.2. Microstructures

The mechanical behaviors presented above were controlled by the microstructures of the 2024 Al alloy at different processing states. To correlate the observed mechanical behaviors with microstructures, we performed systematic TEM and HRTEM investigations on samples at different processing states to reveal their grain structure, evolution of the precipitates and precipitate-dislocation interactions.

Fig. 4 shows the TEM micrograph inside a grain of a 2024 Al alloy sample after SST at 493 °C for 10 h. The grain sizes after SST were determined under TEM as ~5 μm. As shown, this grain is "very clean", attesting to a very low dislocation density. The large rod-like dispersoids were retained from SST and were identified as the orthorhombic T-phase with a composition of $Al_{20}Cu_2Mn_3$ by EDS analysis [37]. The boundaries of the T-phase are very clear and sharp and free of dislocations. The width of the T-phase precipitates is mostly <100 nm and their aspect ratios range from 1 to 7.

These remnant T-phase particles played a critical and positive role in grain refinement and dislocation accumulation during cryo-rolling. Fig. 5 shows a sequence of dislocation accumulation from small rolling strains to large rolling strains. In Fig. 5a, where the sample was rolled to

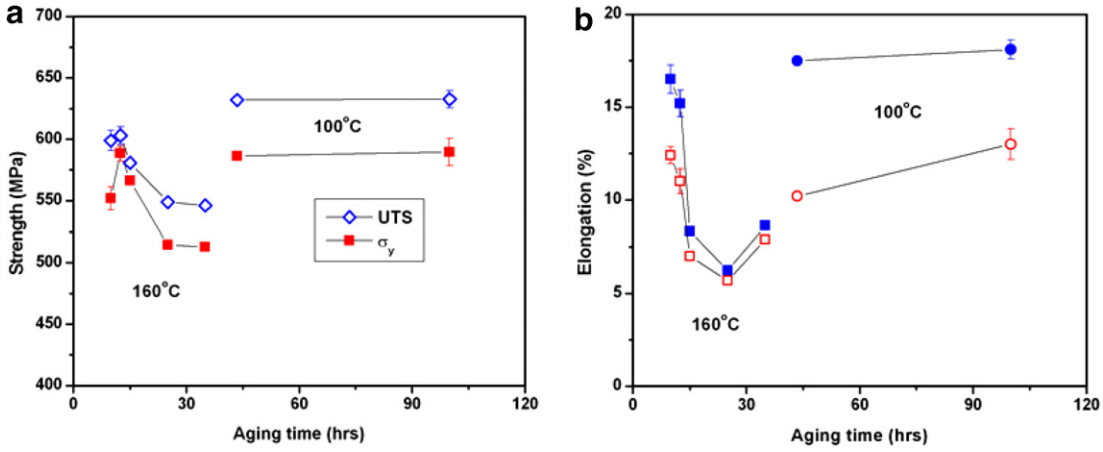

Fig. 3. (a) Tensile strength variations with aging time at 160 and 100 °C. For samples aged at 160 °C, both the yield strength and the UTS reach a peak at $t = \sim 13$ h, then decrease with longer aging times. For samples aged at 100 °C, the yield strength and UTS stayed nearly unchanged from $t = 42$ h to $t = 100$ h. (b) Tensile elongation-to-failure (solid symbols) and uniform elongation (open symbols) variations with aging time at 160 and 100 °C, respectively.

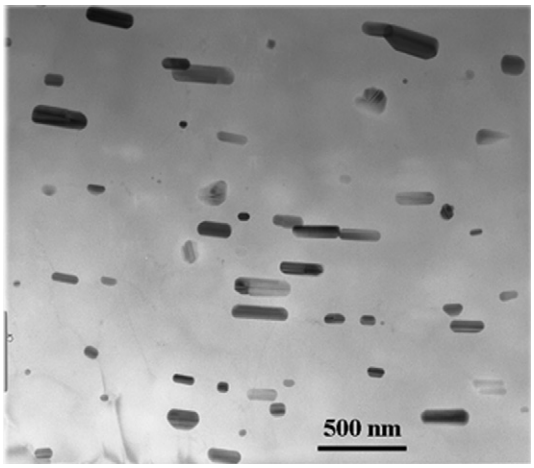

Fig. 4. TEM micrograph of the 2024 Al alloy after solid-solution treatment at 493 °C for 10 h, showing low dislocation density and remnant rod-shaped T-phase.

a strain of ~15%, some dislocations were tangled around the T-phase dispersoids. In Fig. 5b, the rolling strain was increased to ~40%. It is clear that high densities of dislocations were trapped between the T-phase dispersoids, while in areas without T-phase dispersoids, the dislocation density was much lower and large dislocation cells were formed. When the rolling strain was increased to ~80%, dislocations even accumulated in the area away from the T-phase dispersoids and were more homogenously distributed all over the grain.

The microstructure of the SST + CR samples was examined in more detail using TEM. Fig. 6a displays typical bright-field TEM micrographs of an as-rolled sample. The slight contrast difference was caused by small orientation variations among the subgrains. Careful inspection of Fig. 6a suggests that most of the subgrain boundaries are similar to the so-called "non-equilibrium grain boundaries" [38]. Fig. 6b is another bright-field TEM micrograph

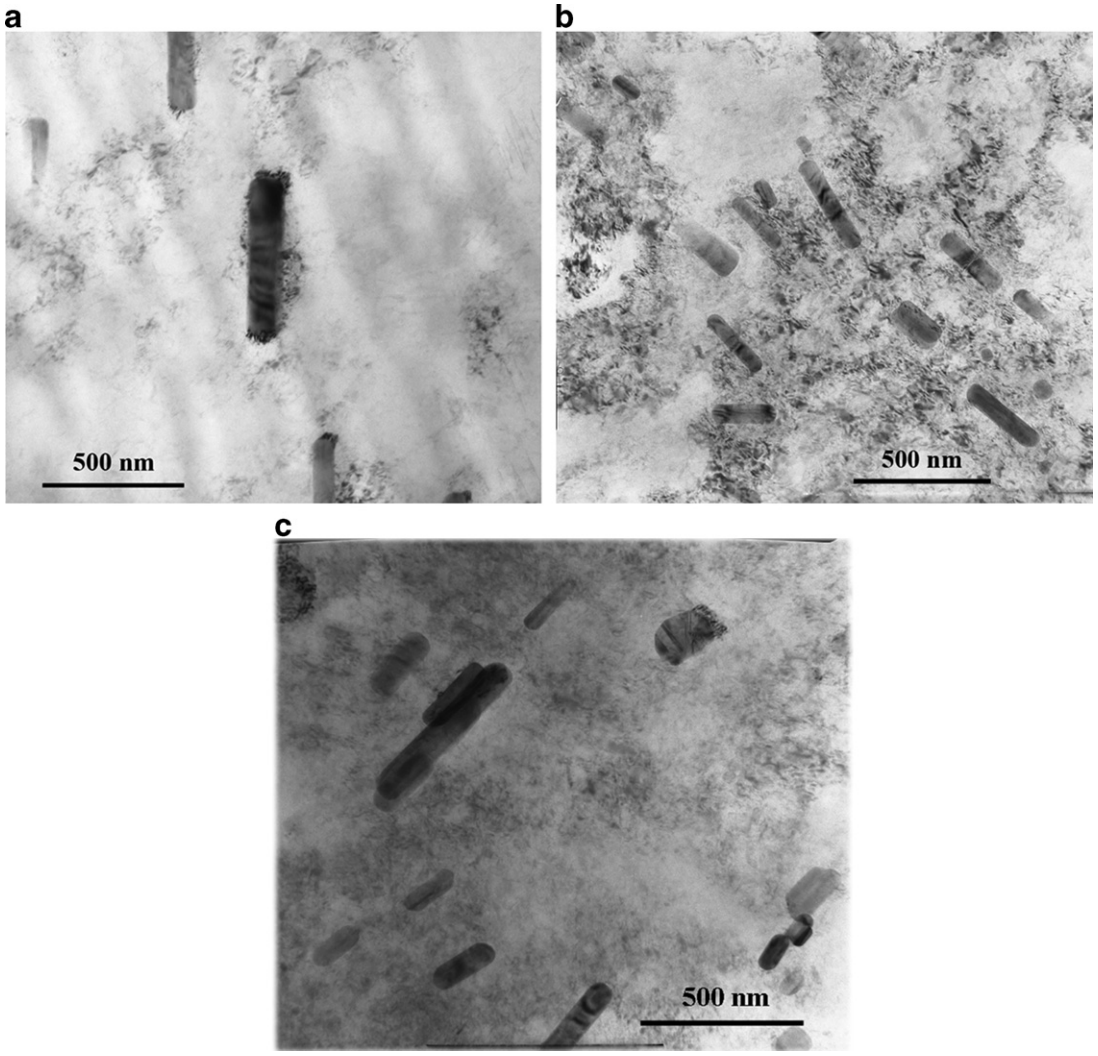

Fig. 5. (a) Dislocations were tangled by T-phase dispersoids after CR to a strain of ~15%. (b) More dislocations were tangled by the T-phase dispersoids and accumulated between the T-phase dispersoids after CR to ~40%. (c) After CR to ~80%, a very high density of dislocations homogeneously accumulated and were stored in the grain/subgrains.

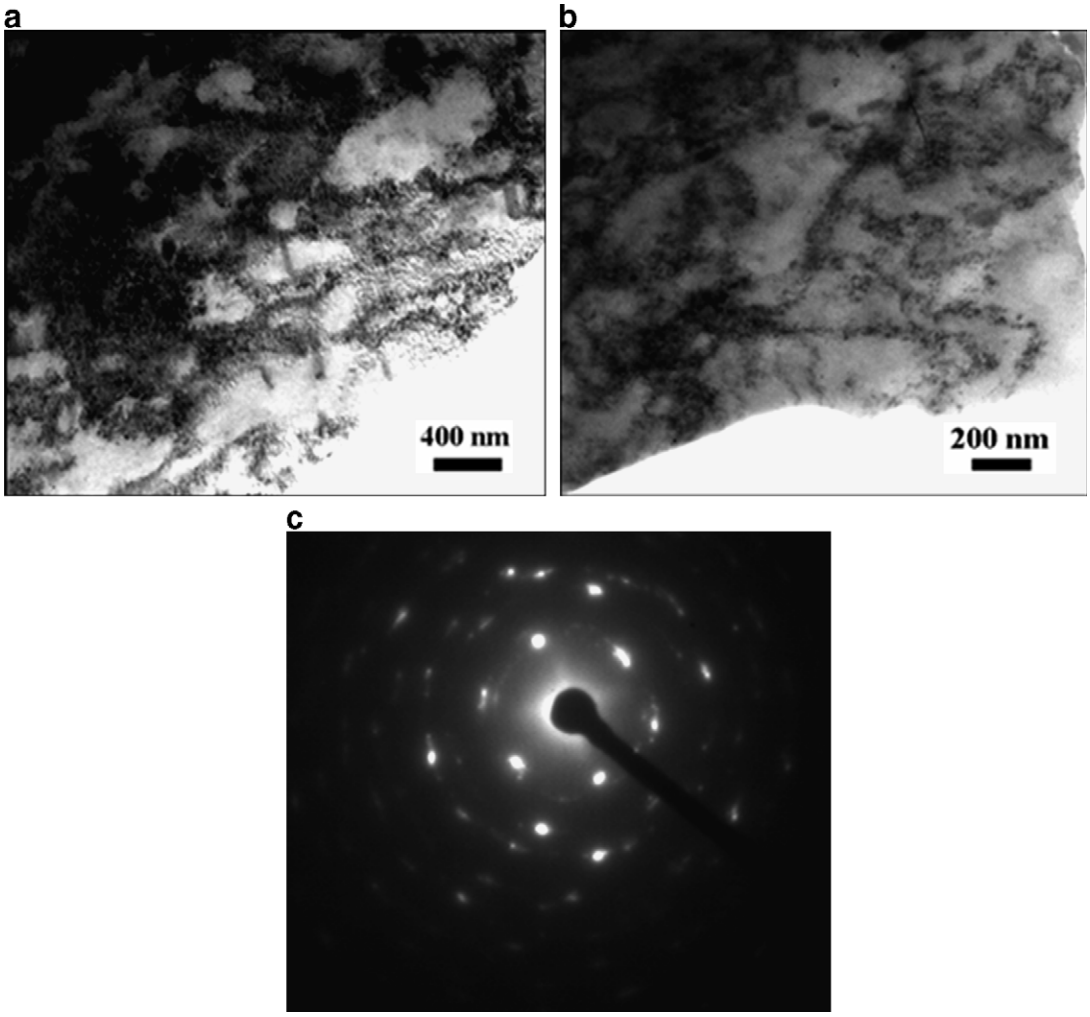

Fig. 6. (a) Bright-field TEM micrograph of CR samples showing the lamellar subgrain structure with submicron sizes. (b) TEM micrograph showing the subgrain morphologies and boundaries. (c) Electron diffraction with a (1 1 0) zone axis showing the refined structure; the aperture size was 1 μm.

that shows more clearly the subgrain morphologies. Some elongated subgrains are revealed with dislocations stuck at the boundaries. Fig. 6c shows the electron diffraction patterns with ⟨1 1 0⟩ zone axis for the cryo-rolled samples. The aperture size used was ~1 μm. It can be seen that the diffracted patterns were distorted into discontinuous rings, suggesting a refined structure, but the misorientations were not large enough to yield continuous rings. The size of the subgrains was refined to 400–800 nm after the cryo-rolling.

Fig. 7 shows the microstructure of a sample that was SST, aged at 160 °C for 10 h and then tensile tested to an elongation of ~30% (corresponding to curve ii in Fig. 2). As shown, similar to many ductile metals, dislocation cells were developed. The typical sizes of dislocation cells are 200–400 nm.

Aging the SST + CR fine-grained samples changed the structures in two aspects. First, the high density dislocations recovered extensively during the course of short aging and grain growth occurred at long aging times due to recrystallization. Secondly, precipitation preferentially took place in locations where the dislocations were heavily tangled, resulting in high density of precipitates. These two structural changes are evidenced in the TEM micrographs shown in Figs. 8 and 9.

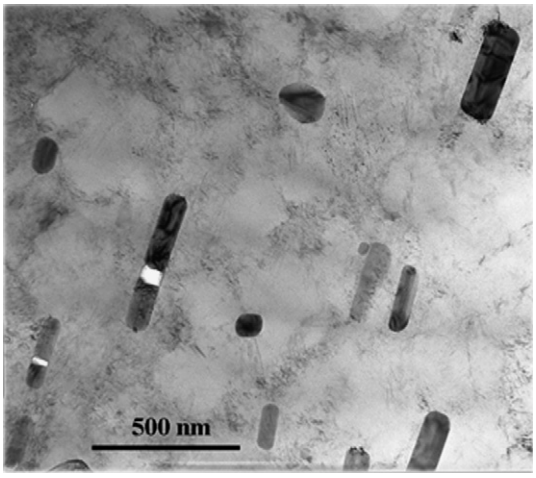

Fig. 7. TEM micrographs of 2024 Al sample that was SST, aged at 160 °C for 10 h and then tensile tested to an elongation of ~30%. Dislocation cells were developed during the tensile test.

Fig. 8a shows the microstructure of a SST + CR + aging sample that was aged at 160 °C for 10 h. It revealed a lamellar subgrain structure that was retained from CR, but the subgrain sizes remained about 400–800 nm, suggesting that recrystallization had not yet commenced. However, when the aging time was increased to 13 h, equiaxied grains ~1 μm in size were observed (Fig. 8b), indicating that recrystallization had occurred. Fig. 8c shows the microstructure of a SST, CR sample that was aged at 100 °C for 100 h. It is evident that recrystallization and some grain growth occurred, which increased the average grain size to 800 nm to 1.5 μm.

The precipitates in a sample aged at 160 °C for 13 h are shown in Fig. 9. As shown in Fig. 9a, densely distributed nano-sized second-phase precipitates had formed during the aging. Fig. 9b shows the second phases under a higher magnification, in which S′ precipitates with two different morphologies can be seen: needle-shaped and lath-shaped, as marked by dotted circles. Both needle- and lath-shaped S′-phase precipitates have a {1 0 0} habit plane with the Al matrix. The width of the needles ranges from 2 to 6 nm and the length ranges from 9 to 17 nm. The average spacing between precipitate particles is ~30 nm. The density of the S′-phase precipitates is estimated from the TEM micrographs as $\sim 1 \times 10^{15}\ m^{-2}$. These precipitates nucleated and distributed homogenously in the grain volume. Fig. 9c is a selected area electron diffraction pattern. The orientation relationship between Al matrix and S′ precipitates is determined as $[\bar{1}00]_{Al}//[100]_S, [021]_{Al}//[010]_S, [01\bar{2}]_{Al}//[001]_S$. Longer time of aging at 160 °C led to precipitate coarsening and a density decrease, which consequently decreased both strength and ductility. In the samples aged at 100 °C for 100 h, S′ precipitates with a size in the range of 10–15 nm had formed, at a higher density of $\sim 4 \times 10^{15}\ m^{-2}$. The interparticle spacing is ~15 nm. The microstructures after different processing procedures are summarized in Table 1.

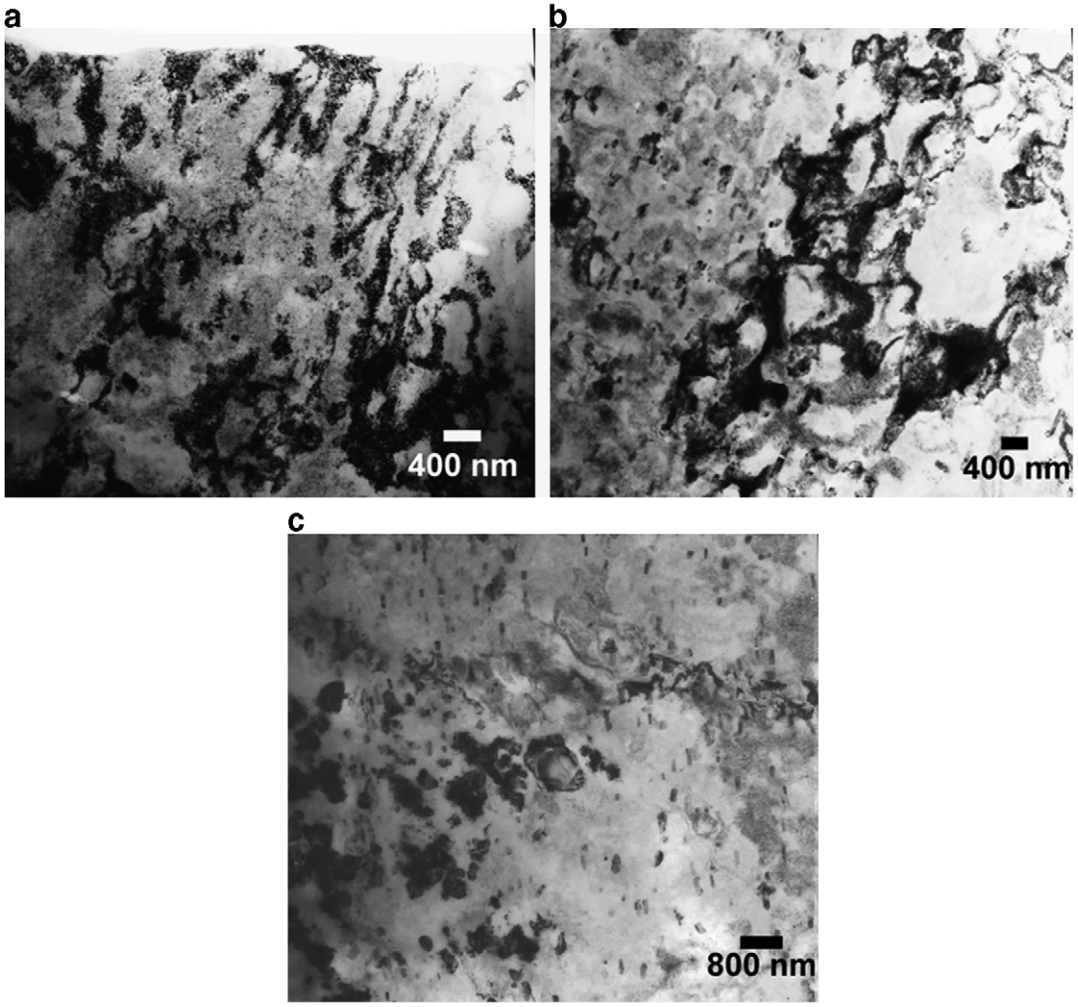

Fig. 8. Bright-field TEM micrographs of SST + CR samples that were aged at: (a) 160 °C for 10 h, where dislocation recovery was observed, but recrystallization has not yet occurred as the grains remained elongated due to the rolling; (b) 160 °C for 13 h, where both recovery and recrystallization have occurred as equiaxied grains have formed; and (c) 100 °C for 100 h, where some extent of grain growth has occurred in addition to recovery and recrystallization.

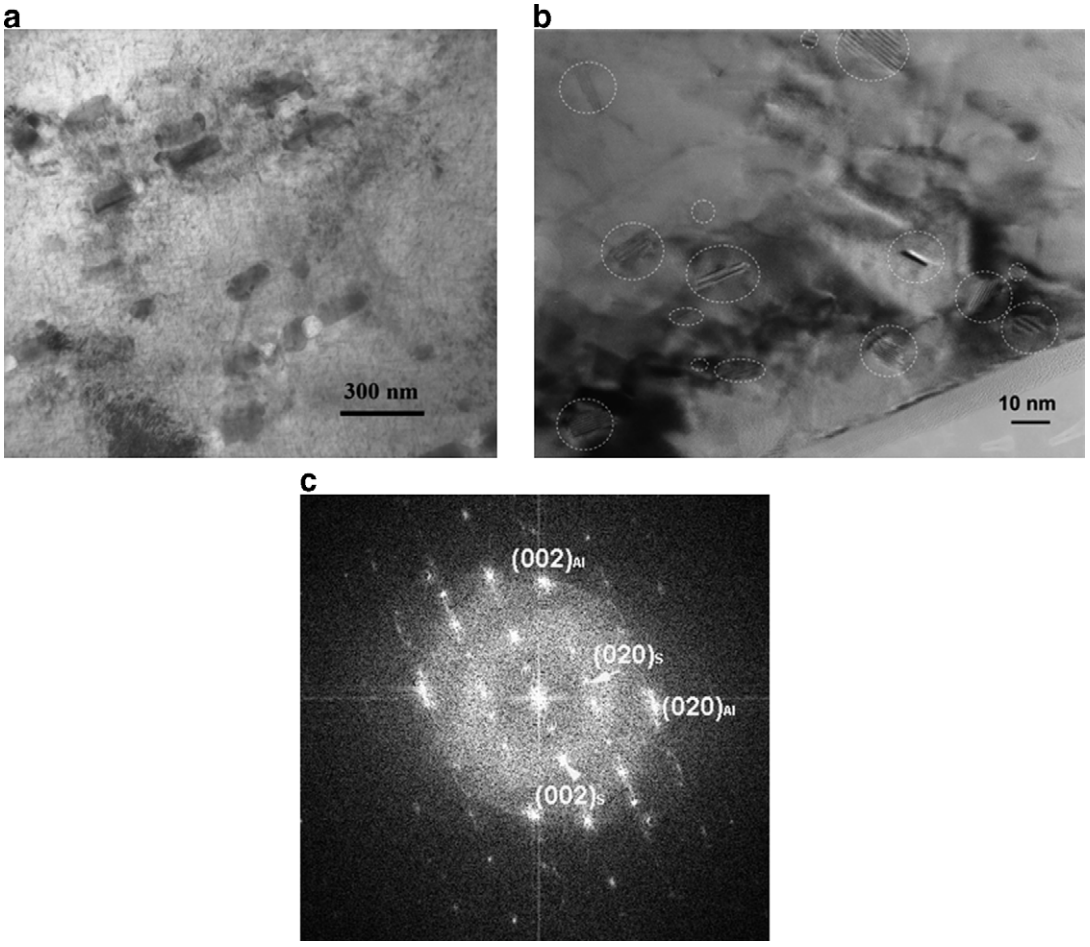

Fig. 9. (a) High density of S′-phase precipitates in the SST + CR samples that were aged at 160 °C for 13 h; the precipitates were homogeneously dispersed in the Al matrix. (b) Needle- and lath-shaped precipitates at a higher magnification. (c) Selected area diffraction pattern from image (b). The subscript "Al" denotes diffraction from the Al matrix and "S" denotes S′-phase. The orientation relationship between Al matrix and S′-phase was determined as: $[\bar{1}00]_{Al}//[100]_S, [021]_{Al}//[010]_S, [01\bar{2}]_{Al}//[001]_S$.

Table 1
Summary of processing states and microstructures of 2024 Al alloys

Aging	Al matrix		Precipitates	
	Shape and state	Grain/subgrain size	Small needles and plates	S′: interparticle spacing/density
160 °C, 10 h	Lamellar grains, dislocation recovery	400 nm ~800 nm	Al_2CuMg S′ phase, orthorhombic, high density	~20 nm/2–2.5 × 10^{15} m^{-2}
160 °C, 13 h	Equiaxed grains, recrystallization	~1 μm	Less high density S′ phase	~30 nm/~1 × 10^{15} m^{-2}
100 °C, 100 h	Large equiaxed grains, recrystallization and grain growth	800 nm ~ 1.5 μm	Higher density S′ phase	10 ~ 15 nm/~4 × 10^{15} m^{-2}

All samples were solution-treated at 493 °C for 10 h and cryo-rolled; all contains remnant orthorhombic T-phase ($Al_{20}Cu_2Mn_3$).

The interaction of S′-phase precipitates with dislocations during tensile testing was investigated using HRTEM. Fig. 10 displays the typical inverse Fourier transformed HRTEM images before and after tensile tests. Shown in Fig. 10a is a typical S′-phase precipitate in the sample prior to tensile testing, which reveals a few dislocations in its vicinity, but no dislocation inside the precipitate. This is because the dislocations generated by CR have been annihilated during the subsequent aging. However, after the tensile test, S′-phase precipitates have entangled many dislocations around them, causing an increase of dislocation density (see Fig. 10b). Some dislocations were also able to cut into the precipitates, as the needle- and lath-shaped S′ precipitates have semi-coherent interfaces with the matrix [39].

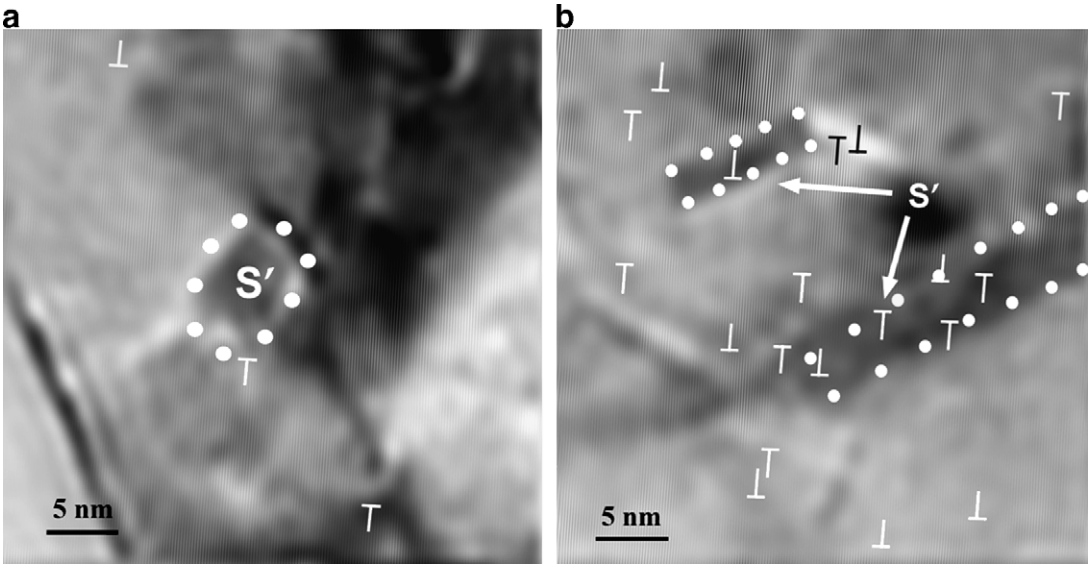

Fig. 10. Typical inverse Fourier transformed HRTEM images of {1 1 1} matrix planes of samples aged at 160 °C for 13 h: (a) before tensile testing and (b) after tensile testing. The white dots denote second S′-phase/matrix interface. Few dislocations were observed in the vicinity of an S′ precipitate particle before tensile testing. In sharp contrast, a high density of dislocations was observed around the S′ precipitate particles after the tensile test. Some dislocations had cut into the S′-phase particles.

4. Discussion

The mechanical behaviors of fine-structured 2024 Al alloys at various processing states are very similar to those reported for 7075 Al alloy at similar states [15,17]. However, precipitation hardening in the 2024 alloy improved the mechanical properties, especially the ductility, more effectively than in the 7075 alloy. Specifically, using the 2024 Al alloy in the state of SST + CR + aging at 100 °C as an example, precipitation hardening increased the yield strength of the SST + CR 2024 alloy sample by 12.4%, which is slightly higher than the 12% obtained in the 7075 alloy [15]. Significantly, precipitation hardening enhanced the uniform elongation of the SST + CR 2024 alloy sample by approximately four times, from 3.2% to 13%, which is much higher than the 2.2 times increase obtained in the 7075 Al alloy. These results indicate that the processing strategy developed in this study is superior to that reported for the 7075 alloy. This superiority is largely derived from the remnant T-phase particles that were not dissolved during the SST.

4.1. Effect of the remnant T-phase particles on microstructures at subsequent processing states

As shown in Fig. 5, the remnant T-phase particles acted to trap dislocations around them, which effectively increased dislocation density during cryo-rolling (Fig. 5a). Consequently, areas with high densities of T-phase particles also have high densities of dislocations (Fig. 5b). More importantly, as the CR strain increased, the high densities of dislocations extended from areas with high density T-phase particles to those with low density T-phase particles (Fig. 5c). The microstructure was also refined as a result of the increased dislocation density (Fig. 6).

Since a high density of dislocations promotes the nucleation of S′-phase precipitates [40,41], the uniformly distributed high density of dislocations led to the uniform precipitation of a high density of nano-sized S′-phase precipitates. As listed in Table 1, the density of S′-phase precipitates in the sample aged at 100 °C for 100 h after SST + CR is $\sim 4 \times 10^{15}$ m^{-2}, which is more than twice the density reported for the 7075 Al alloy [15]. As discussed later, this high density of S′ precipitates led to the superior mechanical properties of the 2024 Al alloy.

4.2. Factors affecting strength

Comparing curve iii with curve ii in Fig. 2 reveals that cryo-rolling significantly increased the strength of solution-treated 2024 Al alloy, but the ductility decreased dramatically. The subsequent aging at 100 °C for 100 h further increased the strength by 12.4% (curve v). This increase was caused by the high density of nano-sized S′-phase precipitates generated during the aging step.

As shown in Fig. 8c, during the aging, three microstructural changes occurred. First, the grain size increased to 800 nm–1.5 μm, which should have decreased the strength of the SST + CR sample and eliminated most the strengthening effect by grain refinement generated during cold rolling. Secondly, the high density of dislocations generated during CR mostly disappeared due to recovery and recrystallization. This should also significantly decrease the strength of the SST + CR sample. Thirdly, a high density of nano-sized S′-phase precipitates was generated during the aging, which should increase the strength. Therefore,

the nano-sized S′-phase precipitates not only compensated for the strength decrease caused by the grain growth and dislocation density decrease, but also further increased the strength by 12.4%, attesting to the effectiveness of a high density of nano-sized S′-phase precipitates in enhancing the strength. This also explains why a previous study did not observe an increase in yield strength after aging, although a significant improvement in ductility was observed [10]. It is likely that the densities of second-phase precipitates were not high enough to overcome the strength decrease caused by the loss in dislocation density and the thermally induced grain growth.

Precipitation strengthening depends on an effective interparticle spacing, L′, i.e., $\tau_p \propto \frac{1}{L'}$ [42], ($L' = r/f$, where r is the average diameter of precipitates and f is the volume fraction of precipitates). Hence, the strength increase due to precipitation can be written as

$$\sigma_p = k\frac{f}{r} \tag{2}$$

Apparently, for a fixed f, an increase of nucleation sites would decrease the precipitate particle size, r; thus the age hardening would be more effective. This is clearly demonstrated in Fig. 2 and Table 1. As listed in Table 1, the SST + CR + aging sample aged at 100 °C for 100 h has smaller and higher density of S′-phase precipitates and, hence, higher strength than the sample aged at 160 °C for 10 h (curves iv and v in Fig. 2). In addition, dislocations inside the semi-coherent S′-phase precipitates (see Fig. 10b) should also increase the strength [43].

4.3. Factors affecting ductility

As shown in Fig. 2, aging at 100 °C for 100 h improved the uniform elongation of the SST + CR sample by ~300% from the as-rolled state (see curves iii and iv). This significant increase in ductility was caused by two microstructural changes that occurred during aging: (i) the dramatic decrease in dislocation density and (ii) the precipitation of a high density of nano-sized S′-phase precipitates. The extremely low dislocation density after aging leaves much room for dislocation accumulation before saturation during tensile testing, which should certainly increase the work-hardening rate. The high density of nano-sized S′-phase precipitates provides effective sites for trapping and accumulating dislocations (see Fig. 10b), which should also increase the work-hardening rate. This is also clearly demonstrated by curves iv and v in Fig. 2, as well as Table 1. As listed in Table 1, the SST + CR + aging sample aged at 100 °C for 100 h (curve v in Fig. 2) has a higher density of S'-phase precipitates than the sample aged at 160 °C for 13 h (curve iv in Fig. 2). This led to improved ductility (including uniform elongation due to sustained work hardening) in the former (curve v) than in the latter (curve iv). In addition, the grain growth during aging should also improve the ductility, but we believe its effect should be secondary. Therefore, all the structural changes that occurred during the aging enhance ductility, which is why we have observed such a dramatic increase in ductility in the 2024 Al alloy after aging.

4.4. Optimization of processing parameters

We attempted to optimize the processing parameters in this study and found that aging at 100 °C for 100 h yielded the best strength and ductility. We also found that the desirable final microstructure for simultaneous high strength and high ductility is a high density of nano-sized second-phase precipitates and low dislocation density. The remnant second-phase particles played a critical role in producing the high density of dislocations during cryo-rolling, which in turn produced a high density of nano-sized second-phase precipitates. This strategy should be applicable to other precipitation-hardened alloys.

We believe the SST parameters should be further investigated to determine the optimum size and distribution of the remnant second-phase particles. Small, uniformly-distributed remnant second-phase particles should be more effective in producing high densities of dislocations during the CR. Another issue that needs further study is how these remnant second-phase particles affect grain refinement during the CR. The grain size obtained in the 2024 Al alloy after CR is not as fine as that reported for 7075 alloy. It is unclear if this is related to the remnant second-phase particles.

5. Conclusions

In this study, we have developed a new processing protocol simultaneously to achieve high strength and ductility of age-hardenable 2024 Al alloy. Unlike previous work, we purposely retained some T-phase particles after the SST, which improved the processibility of the alloy and, more importantly, helped with the generation of a uniformly distributed, high density of dislocations during the subsequent cryogenic rolling at liquid nitrogen temperature. The high density dislocations enhanced the nucleation of the S′-phase during subsequent aging, resulting in a high density of nano-sized S′-phase precipitates, which in turn led to a significant increase in the ability to work harden and consequently higher (uniform) ductility, while modestly increasing strength at the same time. The high density of nano-sized S′-phase precipitates is solely responsible for the strength increase, while both low dislocation density and high density of nano-sized S′-phase precipitates are responsible for the dramatic increase in ductility. This process has produced better ductility than in a preciously reported case [15], in which all second-phase particles were dissolved during SST, attesting to its usefulness. The approach described here may be applicable to many other precipitation-hardening alloys.

Acknowledgements

S. Cheng and E. Ma acknowledge the support at JHU by NSF-DMR 0355395 and R. Zhang for assistance in this research. Y. Zhao and Y.T. Zhu were supported by the DOE-IPP program office. Dr. X.-L. Wang is thanked for helpful discussions.

References

[1] Valiev RZ, Alexandrov IV, Zhu YT, Lowe TC. J Mater Res 2002;17:5.
[2] Wang YM, Ma E, Chen MW. Appl Phys Lett 2002;80:2395.
[3] Wang YM, Chen MW, Zhou FH, Ma E. Nature 2002;419:912.
[4] Höppel HW, May J, Göken M. Adv Eng Mater 2004;6:781.
[5] Cheng S, Ma E, Wang YM, Kecskes LJ, Youssef KM, Koch CC, et al. Acta Mater 2005;53:1521.
[6] Youssef KM, Scattergood RO, Murty KL, Horton JA, Koch CC. Appl Phys Lett 2005;87:091904.
[7] Ma E, Wang YM, Lu QH, Sui ML, Lu L, Lu K. Appl Phys Lett 2004;85:4932.
[8] Han BQ, Lee Z, Witkin D, Nutt S, Lavernia EJ. Metall Mater Trans 2005;A36:957.
[9] Lee YB, Shin DH, Park KT, Nam WJ. Scripta Mater 2004;51:355.
[10] Horita Z, Ohashi K, Fujita T, Kaneko K, Langdon TG. Adv Mater 2005;17:1599.
[11] Wang YM, Ma E. Acta Mater 2004;52:1699.
[12] Kim JK, Kim HK, Park JW, Kim WJ. Scripta Mater 2005;53:1207.
[13] Kim HW, Kang SB, Tsuji N, Minamino Y. Acta Mater 2005;53:1737.
[14] Ma E. JOM 2006;58:49.
[15] Zhao YH, Liao XZ, Cheng S, Ma E, Zhu YT. Adv Mater 2006;18:2280.
[16] Zhao YH, Zhu YT, Liao XZ, Horita Z, Langdon TG. Appl Phys Lett 2006;89:121906.
[17] Zhao YH, Bingert JF, Liao XZ, Cui BZ, Han K, Sergueeva AV, et al. Adv Mater 2006;18:2949.
[18] Zhao YH, Liao XZ, Jin Z, Valiev RZ, Zhu YT. Acta Mater 2004;52:4589.
[19] Horita Z, Fujinami T, Langdon TG. Mater Sci Eng A 2001;318:34.
[20] Kim JK, Jeong HG, Hong SI, Kim YS, Kim WJ. Scripta Mater 2001;45:901.
[21] Kim WJ, Chung CS, Ma DS, Hong SI, Kim HK. Scripta Mater 2003;49:333.
[22] Mao J, Kang SB, Park JO. J Mater Proc Tech 2005;159:314.
[23] Wang LM, Flower HM, Lindley TC. Scripta Mater 1999;41:391.
[24] Cevdet M. Mater Res Bull 2000;35:1479.
[25] Wang SC, Starink MJ. Acta Mater 2007;55:933.
[26] Lumley RN, Morton AJ, Polmear IJ. Acta Mater 2002;50:3597.
[27] Ringer SP, Sakural T, Polmear IJ. Acta Mater 1997;45:3731.
[28] Ferragut R, Somoza A, Dupasquier A, Polmear IJ. Mater Sci Forum 2002;396–402:777.
[29] Gefen Y, Rosen M, Rosen A. Mater Sci Eng 1971;8:181.
[30] Mazzini SG, Caretti JC. Scripta Metall 1991;25:1987.
[31] Cheng S, Ma E. Unpublished work.
[32] Dieter GE. Mechanical metallurgy. 3rd ed. New York: McGraw-Hill; 1986. p. 289–92.
[33] Wang YM, Ma E. Mater Sci Eng A 2004;375–377:46.
[34] Chua BW, Lu L, Lai MO. Phil Mag 2006;86:2919.
[35] Billard S, Fondère JP, Bacroix B, Dirras GF. Acta Mater 2006;54:411.
[36] Han BQ, Lavernia EJ. Adv Eng Mater 2005;7:457.
[37] Wang SC, Starink MJ. Intl Mater Rev 2005;50:193.
[38] Huang JY, Zhu YT, Jiang HG, Lowe TC. Acta Mater 2001;49:1497.
[39] Li BQ, Wawner FE. Acta Mater 1998;46:5483.
[40] Quainoo GK, Yannacopoulos S. J Mater Sci 2004;39:6495.
[41] Chen SP, Kuijpers NCW, van der Zwaag S. Mater Sci Eng A 2003;341:296.
[42] Courtney TH. Mechanical behavior of materials. New York: McGraw-Hill; 1990.
[43] Lee JK. Metall Mater Trans 1998;A29:2039.